

# Crushing of composite structures: experiment and simulation

Francesco Deleo<sup>1</sup>, Bonnie Wade<sup>2</sup>, Paolo Feraboli<sup>3</sup>  
*University of Washington, Seattle, WA 98195-2400*

Mostafa Rassaian<sup>4</sup>  
*Boeing Research & Technology, Seattle, WA*

**A systematic experimental investigation is conducted to evaluate the effect of geometric features on crush behavior. From a carbon/epoxy square tube, individual test segments are machined in order to isolate corner radii and flat sections of varying sizes, for a total of five different test geometries. Laminate thickness, material system, manufacturing process, and test methodology are kept constant throughout the study. For the material system and lay-up considered in this study, fiber tensile fracture and tearing at the corners is responsible for the vast percentage of the energy absorbed, while frond formation and splaying of the flat segments is responsible for a much lower percentage. An analytical expression is derived that accounts for the combined behavior of corner elements and flat segments in the crush behavior of more complex test articles, such as tubes. Explicit dynamic Finite Element Analyses using LS-DYNA's progressive failure MAT54 material model are performed for each of the specimens tested. It is found that the SOFT crash front parameter, a key numerical parameter used to facilitate controlled collapse failure over unstable crushing, is not a constant for the material but it needs to change with each shape tested in order to yield successful simulations. Furthermore, a striking relationship is found between the SOFT parameter and the degree of stability of the section.**

## I. Introduction

The energy-absorbing behavior of composites is not easily predicted due to the complexity of the failure mechanisms that can occur within the material. Composite structures fail through a combination of fracture mechanisms, which involve fiber fracture, matrix cracking, fiber-matrix debonding, and delamination [1]. The brittle failure modes of many polymeric composite materials can make the design of energy-absorbing crushable structures difficult. Furthermore, the overall response is highly dependent on a number of parameters, including the geometry of the structure, material system, lay-up, and impact velocity.

Tubular structures are used by the motorsport and automotive industries as dedicated members to absorb energy in the event of a crash, including automotive-sized front rails. Prepreg or fabric can easily be formed to tubular shapes and is the material of choice for the motorsport industry. Although no standard shape or dimension exists, either circular or square tubes have been traditionally employed, the latter

---

<sup>1</sup> Doctoral student, Department of Aeronautics and Astronautics, University of Washington

<sup>2</sup> President of the AIAA Student Chapter and Undergraduate Research Assistant, Department of Aeronautics and Astronautics, University of Washington

<sup>3</sup> Secretary of AIAA Materials Technical Committee and Assistant Professor, Department of Aeronautics and Astronautics, University of Washington, Box 352400, Seattle, WA, 98195-2400 USA. Tel: 206.543.2170, E-mail: [feraboli@aa.washington.edu](mailto:feraboli@aa.washington.edu)

<sup>4</sup> Technical Fellow, Advanced Structures Technology, Boeing Research & Technology, Seattle, WA

having rounded corners [2]. The vast majority of the research conducted to determine the crush energy absorption of composite materials has focused on thin-wall tubular specimens [1-3]. Only a limited number of attempts have used test specimens of different geometries, and have included both self-supporting shapes, such as semicircular segments [4], channel stiffeners [5], corrugated webs [6], as well as flat plate specimens with dedicated anti-buckling fixtures [7]. The history behind the selection of tubular specimens can be attributed to several reasons: they are self-supporting, they do not require dedicated test fixtures, and they are ideally suited for both quasi-static and dynamic crushing.

On the other hand, the aerospace community has focused mostly on test specimens that resemble subfloor structures, such as floor beams, stanchions and stiffeners. These typically exhibit either a corrugated or channel shape, which are partially self-supporting, therefore do not require a dedicated test fixture, and are open sections, therefore they are more versatile from a manufacturing standpoint, and do not exhibit the hoop fiber constraint as tubular shapes. Bolukbasi and Laananen [5] conducted a systematic comparison of three structural configurations. Flat plates, angle sections, and C-channels were crushed under quasi-static conditions. Unidirectional tape was the material used, and two different lay-ups were considered. The NASA fixture described in [8,9] was used to provide anti-buckling support for the plate specimen. Although the number of specimens tested was limited, as was the selection of laminate lay-ups, it was found that the flat plates tested with the NASA fixture yielded higher SEA (Specific Energy Absorption) measurements than any of the self-supporting specimens, mostly attributable to the overly-constrained nature of the specimen. It was also shown that for both lay-ups tested, corner stiffeners yielded lower SEA than C-channel sections.

The purpose of this study is to identify the effect of cross section geometry on the overall crush behavior of five different specimen shapes, which are all obtained starting from a square tube with rounded corners (Figure 1). These include a small and a large C-channel element, and a small and a large corner element, as well as the square tube itself. The ultimate goal is to isolate the SEA contribution of the corner detail from the total SEA of the section tested. This is achieved by varying the length of the flat segments among the different shapes and then extrapolating the effective, or in-situ, SEA associated to the flat segments, rather than measuring it with complex test fixtures [7].

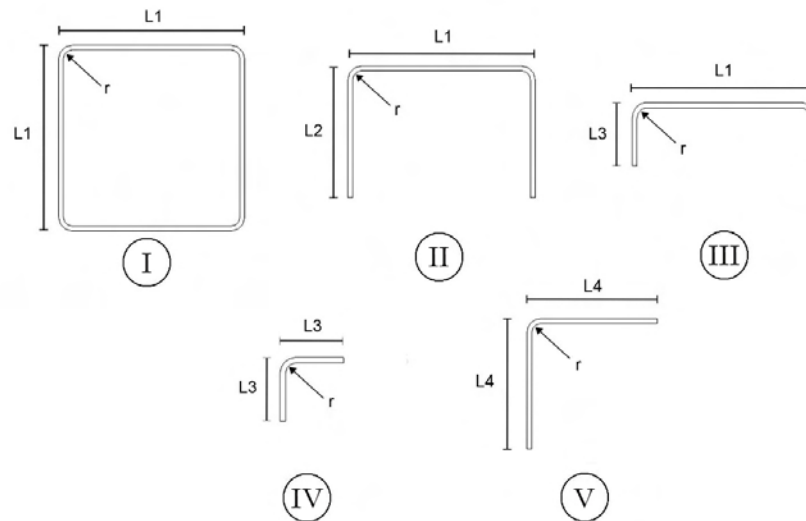


Figure 1. Sketch of cross-section shape and dimensions for all five specimens considered

## II. Experimental

The material system is T700/2510 carbon fiber/epoxy prepreg, supplied by Toray Composites of America. It is a flat woven, 12k tow, plain weave fabric with a 270° F cure resin (132 °C) designated for vacuum bag and oven cure only. The lay-up considered is  $[0/90]_{4s}$ , yielding an average cured laminate thickness of 0.065 in. (1.65 mm). This material is used extensively for general aviation primary structures, and its properties are well documented as part of the FAA-sponsored AGATE Program (Advanced General Aviation Transport Experiment, [10]). These properties are now available in the CMH-17 database [11]. Flat panels as well as tubular shapes are manufactured by the material supplier, Toray Composites of America.

Using an aluminum square tubular mandrel, the square tube is extracted from the mold. After trimming, the length of the specimen is 3.5 in. (88.9 mm). The radius of the mandrel, and hence the inner radius  $r$  of the tube, is 0.175 in. (4.45 mm). The cross section of the tube has outer dimensions  $L1 \times L1$  (Figure 1, I) and a total perimeter of  $S_I$  (Figure 2, I). In order to obtain the other four shapes considered in this study, a portion of the square tube specimens are cut with a diamond-coated disk saw. With a single cut performed off-axis on the square cross-section (Figure 3, I) the large and the small C-channel sections are obtained (Figure 3, II and III respectively). The large C-section has dimensions  $L1 \times L2$ , while the small C-channel has outer dimensions  $L1 \times L3$ , where  $L3$  is the given by  $L1-L2$  (Figure 1, II and III). The total perimeters for the large and small C-channels are indicated as  $S_{II}$  and  $S_{III}$  respectively (Figure 2, II and III). In order to obtain the fourth specimen, a second cut is performed on a portion of the small C-channels previously obtained. The cut is performed off-axis (Figure 3, IV), and it enables for isolating a single corner element. The small corner element has outer dimensions  $L3 \times L3$  (Figure 1, IV), and a perimeter indicated by  $S_{IV}$  (Figure 2, IV). The fifth and last specimen, the large corner element, is obtained by performing two cuts on the original square section I (Figure 3, V), in the proximity of two opposing corners. The specimen has outer dimension  $L4 \times L4$  (Figure 1, V), and section length  $S_V$  (Figure 2, V). Tables I and II shows in detail the list of parameters introduced and the associated numerical values.

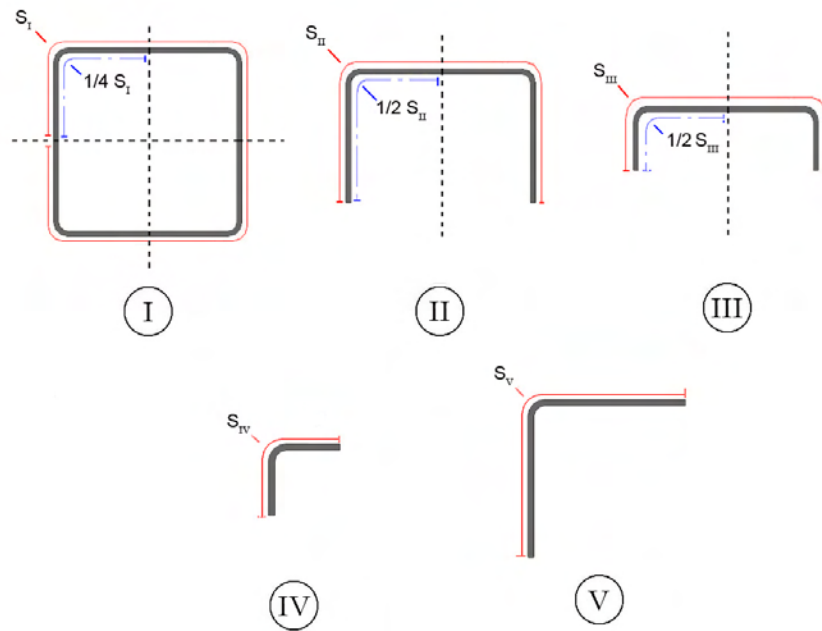


Figure 2. Illustration of the concept of section length for each geometry considered, and portion of such length influenced by a single corner detail.

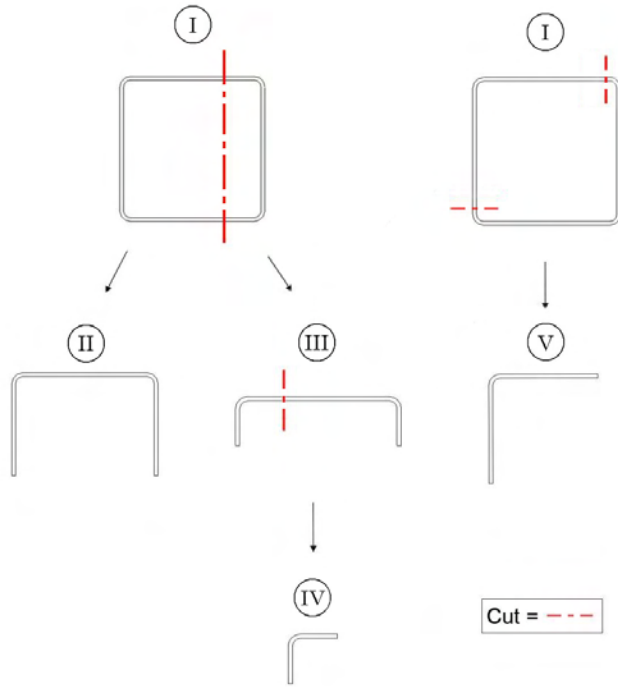


Figure 3. Schematic of machining operation performed to obtain test specimens II through V beginning from specimen I.

Table I. Summary of the five specimens considered and associated key geometric features.

Specimen No.	Shape	Outer Dimensions	Section Length	Portion of cross section affected by one corner
I	Tube	L1 x L1	$S_I$	$\frac{1}{4} S_I$
II	Large Channel	L1 x L2	$S_{II}$	$\frac{1}{2} S_{II}$
III	Small Channel	L1 x L3	$S_{III}$	$\frac{1}{2} S_{III}$
IV	Small Corner	L3 x L3	$S_{IV}$	$S_{IV}$
V	Large Corner	L4 x L4	$S_V$	$S_V$

Table II. Summary of parameters and associated numerical values used in this study.

Parameter	Value
L1	2.50 in. (63.5 mm)
L2	1.75 in. (44.5 mm)
L3	0.75 in. (19.0 mm)
L4	2.00 in. (50.8 mm)
r	0.175 in. (4.45 mm)
t	0.065 in. (1.65 mm)
S <sub>I</sub>	10.50 in. (266.7 mm)
S <sub>II</sub>	5.75 in. (146.0 mm)
S <sub>III</sub>	3.75 in. (95.3 mm)
S <sub>IV</sub>	1.25 in. (31.75 mm)
S <sub>V</sub>	4.50 in. (114.3 mm)
$\Delta s'$	0.75 in. (19.0 mm)
$\Delta s''$	1.00 in. (25.4 mm)
$\Delta s'''$	1.60 in. (40.6 mm)
$\rho$	1.52 g/ cm <sup>3</sup>

Each of the five sections considered in this study is comprised of one or more corner details, and additional segments of flat material. If the small corner detail, specimen IV, is used as the repetitive unit, each cross-section can be subdivided into half- or quarter-sections that are influenced by a single corner detail. The purpose of this effort is to be able to measure the SEA and crush behavior of a stand-alone corner element, and then extrapolate the actual in-situ SEA and crush behavior of the flat sections, which is otherwise difficult to assess experimentally [7-9].

To that extent, the square tube cross-section can be subdivided in a quarter-section, comprised of the corner detail of perimeter S<sub>IV</sub>, and two additional flat segments on both sides of the corner, each of length  $\Delta s'$  (Figure 4, I). This quarter section represents the portion of the square cross-section that is influenced by a single corner detail, since the double symmetry accounts for the other three corner elements. For the large C-channel, the half-section comprises the corner detail of perimeter S<sub>IV</sub>, same as the corner element specimen, and two additional flat segment of total length  $\Delta s'$  and  $\Delta s''$  (Figure 4, II). This half section represents the portion of the large C-channel cross-section that is influenced by a single corner detail, since symmetry accounts for the other corner element. Similarly, the small C-channel can be subdivided into a half-section, comprised of the corner detail of perimeter S<sub>IV</sub>, same as the corner element specimen, and one additional flat segment of length  $\Delta s'$  (Figure 4, III). Lastly, the large corner element can be also subdivided into a small corner element of perimeter S<sub>IV</sub>, and two additional flat segments, each of length  $\Delta s'''$  (Figure 4, V).

For each of the specimens (Figures 2, 4), the length of the cross-section influenced by a single corner ( $S_i$ ) is defined as:

$$S_i = \begin{cases} \frac{1}{4} S_I & \text{for specimen I} \\ \frac{1}{2} S_{II} & \text{for specimen II} \\ \frac{1}{2} S_{III} & \text{for specimen III} \\ S_{IV} & \text{for specimen IV} \\ S_V & \text{for specimen V} \end{cases} \quad (1)$$

The remaining portion of the cross-section is comprised of flat segments (Figure 6), which are defined as:

$$\Delta S = S_i - S_{IV} \quad (2)$$

where:

$$\Delta S = \begin{cases} 2\Delta S' & \text{for specimen I} \\ \Delta S' + \Delta S'' & \text{for specimen II} \\ \Delta S' & \text{for specimen III} \\ 0 & \text{for specimen IV} \\ 2\Delta S''' & \text{for specimen V} \end{cases} \quad (3)$$

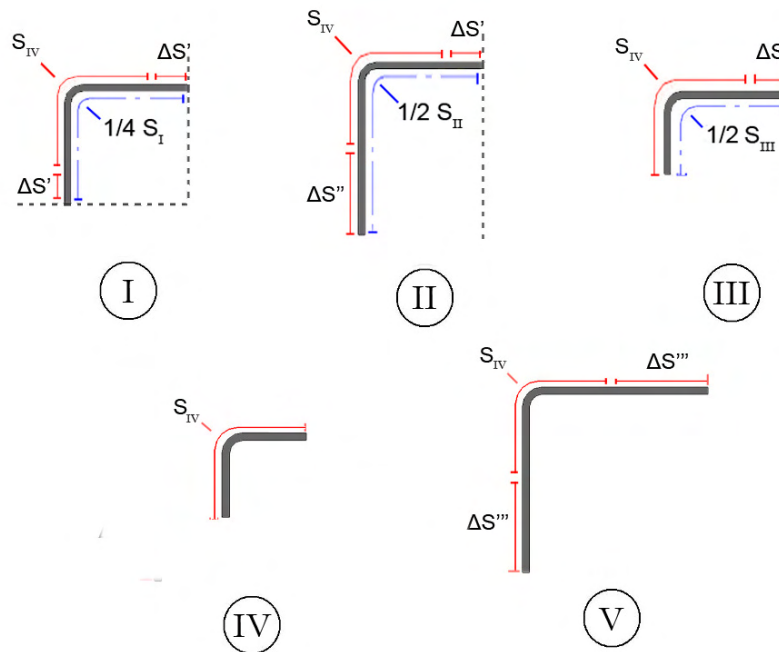


Figure 4. Subdivision of section length into a corner detail and portion of flat segments, for each of the five specimen cross-section geometries considered.

Numerical values for all the quantities reported in eq. 2 and eq. 3 are summarized in Table II. The coupons are 3.5 in. long (88.9 mm), and their width varies according to geometry. The trigger is 45-degree single chamfer on the outside edge, as used in most studies to initiate crushing in self-stabilizing structures. All tests are conducted at a quasi-static rate of 2.0 in./ min (50.8 mm/min), which is noticeably below any dynamic effect previously reported for modern systems [1,6], approximately 40 in./sec (1.0 m/sec). Specimens rest on a polished hardened steel surface. All section specimens except for the tube are potted into an epoxy resin base in order to provide stability during crushing; hence their effective length is reduced by at least 0.5 in. (12.5 mm). Pictures of the test specimens before and after crushing are shown in Figures 7 – 11.

The ability of a material to dissipate energy can then be expressed in terms of SEA, which has units of J/g, and indicates a number, which for composites is usually comprised between 15 and 100 J/ g. Setting the mass of structure that undergoes crushing as the product of stroke  $l$ , cross-sectional area  $A$ , given by the product of thickness  $t$  and section length  $S$ , and density  $\rho$ :

$$SEA = \frac{EA}{\rho \cdot A \cdot l} = \frac{\int F \cdot dl}{\rho \cdot t \cdot S \cdot l} \quad (4)$$

In the present study, density and thickness remain constant for all specimen geometries, thereby leaving as only variables of interest the section length  $S$ . Summary of the test results are reported in Table III. For each of the specimen geometries listed, six test repetitions are performed, and the variation among these repetitions is captured via the Coefficient of Variation (CoV).

All specimens tested in this study crush in a stable manner, Figures 4-8, exhibiting frond formation and bending, particularly specimens II-V. The square tube, specimen I, exhibits an accordion-type of crushing, comprised of a succession of local segments folding on each other. It should be observed that the predominant failure mode at the corner is tearing fracture of the woven fiber tows, while in the flat segments it is lamina bending of the fronds.

Table III. Summary of crush test results for all five specimen geometries

Specimen No.	Shape	Peak Force (kN)	Average Crush Force (kN)	Crush Efficiency	Average SEA (J/g)	CoV (%)
I	Tube	39.9	23.8	1.68	36.9	10
II	Large Channel	21.6	13.0	1.66	36.8	9
III	Small Channel	17.1	10.7	1.60	42.7	3
IV	Small Corner	7.5	4.9	1.53	62.3	11
V	Large Corner	15.3	9.4	1.63	31.6	8

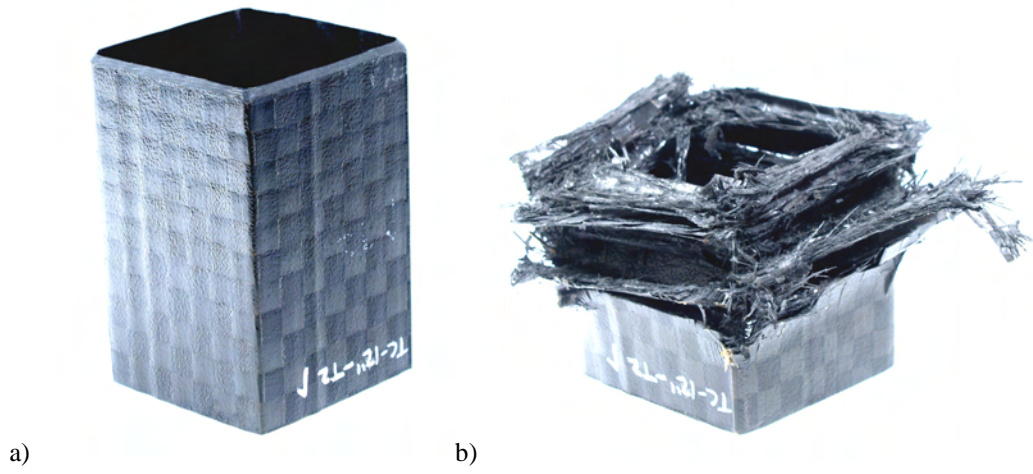


Figure 4. Square tube, specimen I, before (a) and after crush testing (b).

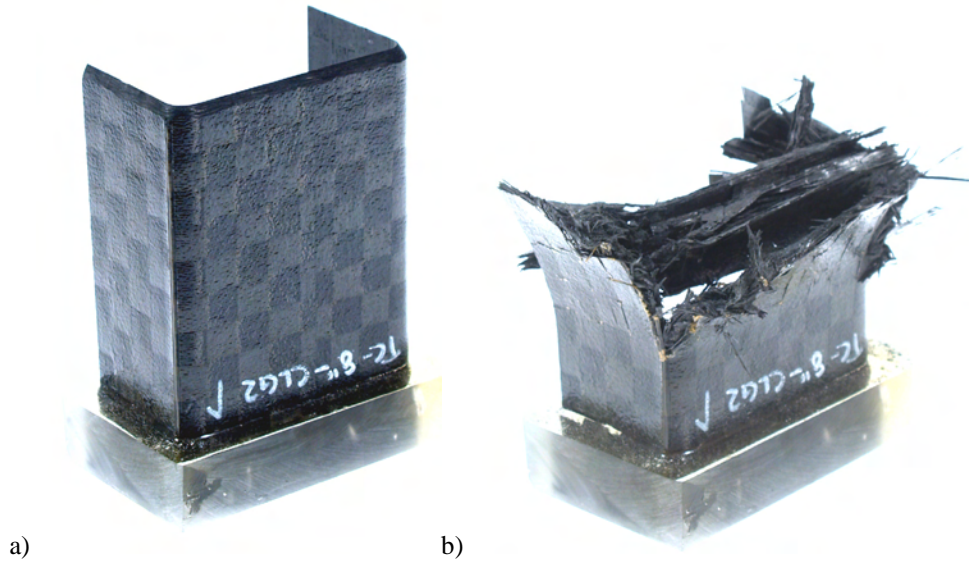


Figure 5. Large C-channel, specimen II, before (a) and after crush testing (b).



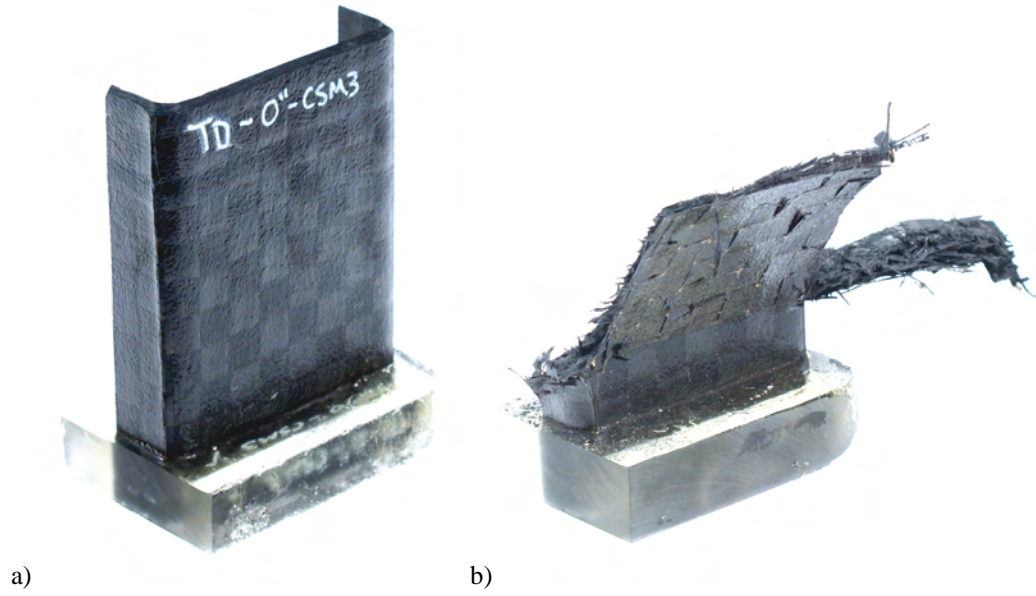


Figure 6. Small C-channel, specimen III, before (a) and after crush testing (b).

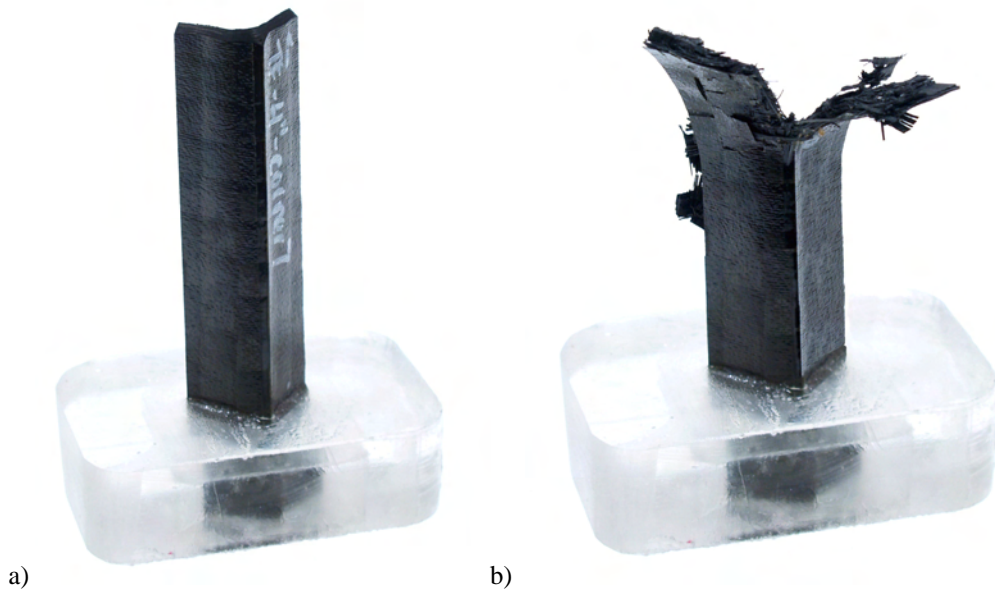


Figure 7. Small corner element, specimen IV, before (a) and after crush testing (b).

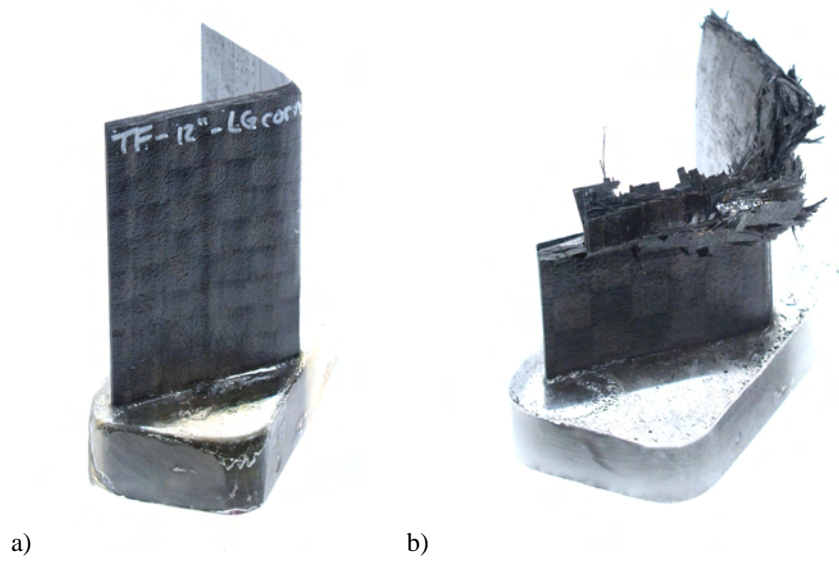


Figure 8. Large corner element, specimen V, before (a) and after crush testing (b).

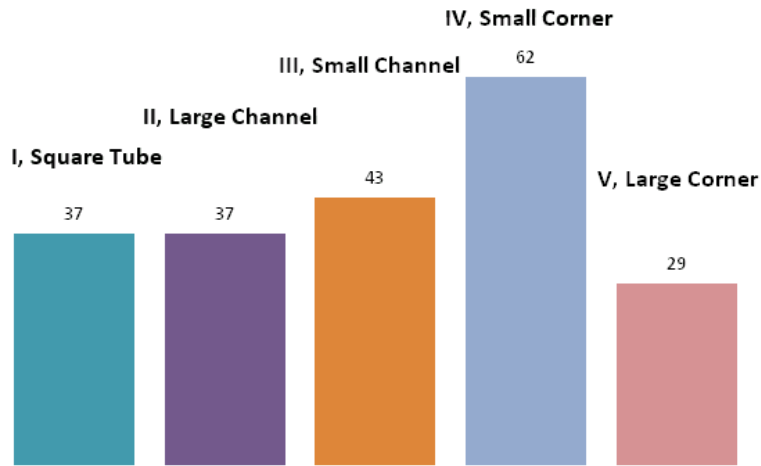


Figure 9. Summary of average SEA results in J/g for all five specimens tested.

In general, it can be seen from Figure 9 that the small corner element exhibits a much higher SEA than the other specimens, followed by the small and large C-channels, the square tube and, lastly, the large corner element. The small corner, exhibiting the least amount of flat segments in its cross section, is therefore the most efficient in dissipating energy per unit mass of material crushed, and this can be attributed to the tearing failure mechanism observed. On the other hand, the large corner is the least efficient, exhibiting the most amount of flat segments in its cross section, and this can be attributed to the frond bending failure mechanism observed. The  $SEA_i$  for each shape can be subdivided into two components, one associated with the corner detail, obtained from testing a corner element and denoted  $SEA_{IV}$ , and one associated to the remaining flat segments, and denoted  $SEA_f$ . These SEA contributions are

weighed based on the ratio of the lengths of corner detail ( $S_{IV}$ ) with respect to the total length of the section ( $S_i$ ), and of the remaining flat segments ( $\Delta S$ ) with respect to the total length of the section ( $S_i$ ):

$$SEA_i = \left( \frac{S_{IV}}{S_i} \right) SEA_{IV} + \left( \frac{\Delta S}{S_i} \right) SEA_f \quad (5)$$

If eq. 5 is solved for the unknown value of  $SEA_f$  since all other quantities are either known or can be measured experimentally, it is possible to extrapolate the in-situ value of the SEA associated with flat sections, like the ones that form the fronds observed in splaying failure. The average value obtained this calculation is  $SEA_f = 16.3 \text{ J/g}$ , which is much lower than the average  $SEA_{IV} = 62 \text{ J/g}$  recorded during the crushing of the corner elements. Although there is evident variation in the results, it is consistent with the CoV measured between repetitions. In conclusion, although the corner element exhibits a higher measured SEA than any of the other shapes tested, the contribution of the flat sections cannot be neglected.

From the study it is possible to note that the degree of curvature greatly influences the energy absorption behavior: the more contoured the specimen cross-section, the higher the energy dissipated per unit mass of material. This observation becomes evident in Figure 20, which plots the variation of SEA with respect to the dimensionless index  $\phi$ , which is an indicator of the degree of curvature of the cross-section, and is given by:

$$\phi = \frac{l}{S_i} = \frac{\pi \cdot r}{2 \cdot S_i} \quad (6)$$

where  $l$  is the arc length, given by the product of the radius  $r$  and the angle  $\pi/2$ , and  $S_i$  is length of the cross section influenced by the corner, as defined in eq. (1).

Segments of cross-section characterized by changes in curvature, such as corners, are much more efficient in absorbing energy than sections with long flat segments, as shown in Figure 10, where there appears to be a linear trend between SEA and the dimensionless parameter  $\phi$ .

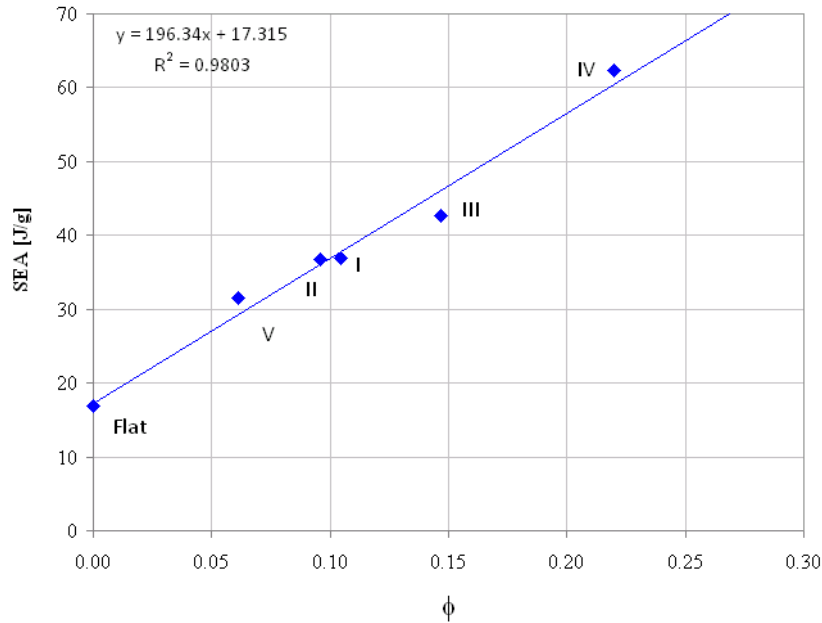


Figure 10. SEA variation with  $\phi$ , which is an indicator of curvature per unit length of cross-section for all specimens tested.

This in turn implies that if a test specimen, such as a small corner element, is used to measure the SEA, it may overestimate the energy dissipation of a structure comprised of corners and flat segments. At the same time, ignoring the contribution of these flat segments and considering the SEA of the corner details alone will underestimate the energy dissipation of such structure. Therefore the results support the development of one or more test methods to measure the SEA for flat plate specimens, and for portions of structures characterized by changes in curvature. The results also support the concept that crushing is a not just a material property but a combined material/structure property.

### III. Analytical

Composite constitutive models implemented in commercial explicit finite element (FE) programs are continuum mechanics models. Composites are modeled as orthotropic linear elastic materials within a failure surface. The exact shape of the failure surface depends on the failure criterion adopted in the model. The failure criteria for laminated composites are typically strength based. Beyond the failure surface, the appropriate elastic properties are degraded according to the assigned degradation laws. By means of stiffness degradation, the nonlinear and softening responses of a composite material after its initial failure are described mathematically.

Depending upon the specific degradation law used in a model, the continuum mechanics models can be further divided into two broad categories. They are either progressive failure models or continuum damage mechanics models (see Table IV). Progressive failure models use a ply discount method to degrade material properties. When an element reaches complete failure, it is eroded and it simply disappears. The failure morphology for MAT54 due to crushing is therefore of little graphical interest, as it does not exhibit frond formation or elements being ejected, such as for example MAT58.

At the failure surface, the values of the appropriate elastic properties of the ply at the material direction are degraded from its undamaged state to a fully damaged state, which is often considered a complete loss and assigned a value of zero. The so-called progressive failure is realized through ply-by-ply failure in the perspective of a laminate. Progressive failure models have shown success [6] in axial crush simulations of composites exhibiting brittle fracture, such as unidirectional and small-tow prepreg.

Table IV. Summary of composite material models available in the commercial explicit FE code LS-DYNA.

MAT	Title	Brick	Shell	T-shell	Degradation Law
22	Composite Damage	y	y	y	Progressive failure
54/55	Enhanced Composite damage		y		Progressive failure
58	Laminated Composite Fabric		y		Damage Mechanics
59	Composite Failure	y	y		Progressive failure
161	Composite MSC	y			Damage Mechanics
162	Composite MSC	y			Damage Mechanics

MAT 54 material model is a progressive failure model within the commercial software LS-Dyna, which uses the Chang-Chang failure criterion. Failure can occur when one of the following strength criteria is exceeded [12, 13]:

- Tensile failure in axial (1-) direction:

$$\sigma_{11} > 0 \quad \rightarrow \quad s_f = \sqrt{\left(\frac{\sigma_{11}}{X_t}\right)^2 + \beta \left(\frac{\sigma_{11}}{S_0}\right)} \quad \begin{cases} \geq 1 & \text{failed} \\ < 1 & \text{elastic} \end{cases}$$

If failure occurs: E1, E2, G12, v21 and v12 are set to zero on the ply that failed.

- Compressive failure in axial (1-) direction:

$$\sigma_{11} < 0 \quad \rightarrow \quad s_c = \frac{\sigma_{11}}{X_c} \quad \begin{cases} \geq 1 & \text{failed} \\ < 1 & \text{elastic} \end{cases}$$

If failure occurs: E1, v21 and v12 are set to zero on the ply that failed.

- Tensile failure in transverse (2-) direction:

$$\sigma_{22} > 0 \quad \rightarrow \quad s_m = \sqrt{\left(\frac{\sigma_{22}}{Y_t}\right)^2 + \frac{s_{12}^2 + \frac{3}{4}\alpha v_{12}^4}{2G_{12} + \frac{3}{4}\alpha S_0^4}} \quad \begin{cases} \geq 1 & \text{failed} \\ < 1 & \text{elastic} \end{cases}$$

If failure occurs: Eb, Gab and vba are set to zero on the ply that failed.

- Compressive failure in transverse (2-) direction:

$$\sigma_{22} < 0 \quad \rightarrow \quad s_d = \sqrt{\left(\frac{\sigma_{22}}{2S_0}\right)^2 + \left[\left(\frac{Y_c}{2S_0}\right)^2 - 1\right] \left(\frac{\sigma_{22}}{Y_c}\right) + \left(\frac{\sigma_{22}}{S_0}\right)^2} \quad \begin{cases} \geq 1 & \text{failed} \\ < 1 & \text{elastic} \end{cases}$$

If failure occurs: Eb, Gab, vba and vab are set to zero on the ply that failed.

In the above equations, Xt is the longitudinal tensile strength, Xc is the longitudinal compressive strength, Yt is the transverse tensile strength, Yc is the transverse compressive strength and Sc is the shear strength. The material properties as well as the parameters  $\alpha$  and  $\beta$  are listed in Table IV. All parameters are kept constant between the models of the various geometries, except for the SOFT parameter, as described subsequently. Beside the Chang-Chang strength criterion, a ply can be removed when the strain exceeds one of the ultimate strains. A ply can also be removed if failure does not occur by any of the above reasons within a cycle time smaller than TFAIL, and the element is eliminated by time out. The other parameters described in Table V are:

- SOFT is the crash front parameter is a softening reduction factor for material strength in the row of elements immediately following that currently undergoing crushing. The default value is 1, which means that the elements are pristine, or retain 100% of their strength. A SOFT value of 0.6 indicates that the row of elements following the crashfront is set to retain only 60% of the pristine strength. It acts as a damage zone by assuming that the row of elements right after to the crashfront undergoes a partial state of damage even before it becomes the crashfront.
- Alpha is the shear stress parameter for the non linear term.
- Beta ( $\beta$ ) is the weighting factor for shear term in tensile fiber mode. It ranges from 0 to 1. For  $\beta = 1$ , the failure criteria of Hashin [8] is applied in the fiber tensile mode. When  $\beta = 0$ , Equation 5 reduces to the maximum stress criterion.

- EFS is effective failure strain. In this study, EFS was set to zero and was hence not considered by the material model. If EFS was set to a positive value, failure occurs if the effective strain is greater than the EFS value.
- DFAILM is the maximum strain for matrix straining in tension or compression.
- DFAILS is the maximum shear strain.
- DFAILT is the maximum strain for fiber tension.
- DFAILC is the maximum strain for fiber compression.
- TFAIL is the time step size criteria for element deletion. In this study, TFAIL was assigned a value less than 0.1, hence the element is deleted when its time step is smaller than the given value.

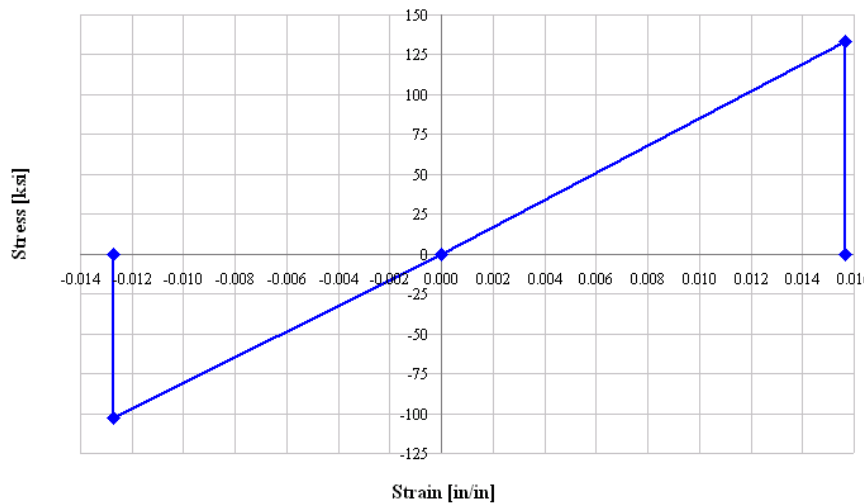


Figure 11. Tension-compression stress-strain curve for the material in this study.

The FE model is discretized with elements of 0.1 in. x 0.1 in. (2.54 mm x 2.54 mm). Although the simulation is highly mesh size dependent, once it is found that the above element size worked well for all geometries, the mesh size is kept constant throughout the study. A row of trigger elements is used to represent the physical chamfer that is used in the experiment to initiate crushing. The trigger is modeled as a separate row of elements, comprised of the same material properties as the bulk of the specimen, but with a reduced thickness: 0.02 in. instead of 0.065 in. (0.5 mm vs. 1.65 mm).

The loading platen is modeled as a rigid part in steel of 0.3 inches in width, and the contact between the specimen and the plate is set to “Rigid Nodes to Rigid Body”. The nodes of the bottom row were fixed against vertical displacements, and the loading plate is set to move with an initial vertical velocity 150 in./sec (3.8 m/sec). Although stiffness of the contact force-penetration curve has a great effect on the results, once one is found that works well for all geometries, it is kept constant throughout the study.

An 600 Hz SAE filter is applied to raw numerical results. A filter is needed because of the accentuated sawtooth pattern of the unfiltered curve, which is due to the incremental failure of the rows of elements.

Table V. MAT 54 input properties of all geometries

Symbol	Title	Value
SOFT	Crash front parameter	...
Alpha	Shear stress parameter for non linear terms	0.3
Beta	Weighting factor for shear term in tensile fiber mode	0.5
EFS	Effective failure strain	0
DFAILM	Max strain for matrix straining in tens. and comp.	0.013
DFAILS	Max shear strain	0.03
DFAILT	Max strain for fiber tension	0.02
DFAILC	Max strain for fiber compression	-0.013
TFAIL	Time step size criteria for element deletion	1.153 E-9
Shell element size	In.	0.1
Contact Type	Rigid nodes to rigid body	
Xc [ksi]	Longitudinal compressive strength	103
Xt [ksi]	Longitudinal tensile strength	132
Yc [ksi]	Transverse compressive strength	140
Yt [ksi]	Transverse tensile strength	112
Sc [ksi]	Shear strength	19
Ex [Msi]	Longitudinal elastic modulus	8.11
Ey [Msi]	Transverse elastic modulus	7.89
pryx	Poisson's ratio YX	0.043
Gxy [Msi]	Shear Modulus XY	0.609
Gyz [Msi]	Shear Modulus YZ	0.609
Gzx [Msi]	Shear Modulus ZX	0.609

For each geometry, the comparison between FE model and experiment is performed on the basis of the SEA value and of the shape of the load-displacement curve, and specifically of the initial slope, peak load and average load. As mentioned, all parameters in Table V are kept constant for all five specimen geometries except for the SOFT parameter. Beginning from specimen I, the square tube, it is found that the value assigned to the SOFT parameter has the most dramatic influence on the overall simulated crush response, as shown in Figures 12-14. For SOFT values that are too high, which means that the strength of the element row following the crush front is not reduced enough, crushing is not stable. Upon loading, stress builds up and eventually leads to failure at a point away from the crush front. In Figure 12, with a SOFT value of 0.64, instability occurs very early into the crushing, at 2.446 msec. Lowering the SOFT parameter by trial and error it is possible to continue the crushing for a longer period of time. With a SOFT value of 0.3, crushing progresses until 3.728 msec, at which point instability occurs and the specimen fails catastrophically, Figure 13. By further lowering the SOFT parameter, the crushing becomes stable with a value of 0.15, and instability does not occur. However, the load-displacement (L-D) curve is much higher than the one measured experimentally. Further reducing the SOFT to 0.08, again by trial and error, it is found that the L-D curve matches the experimental one very well, Figure 14. Example of the L-D curves obtained for SOFT values of 0.64, 0.3, 0.15 and 0.08 are shown in Figure 15.



Figure 12. Example of an unstable crushing of the tubular shape with  $\text{SOFT}=0.64$  Buckling starts after 2.446 millsec at a displacement of 0.3669 inches.

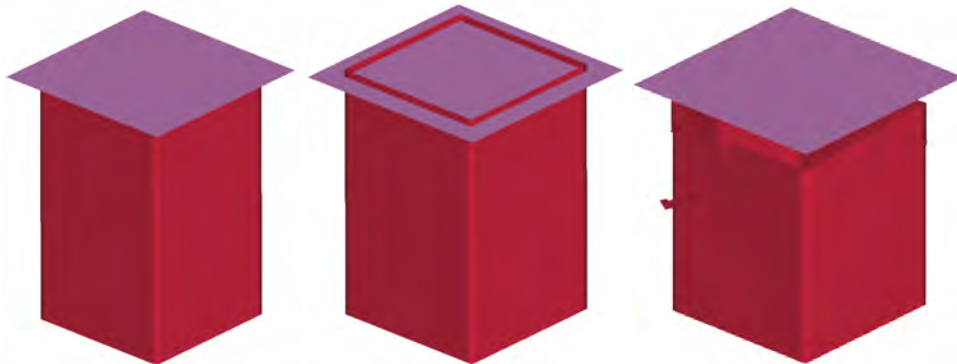


Figure 13. Example of an unstable crushing of the tubular shape with  $\text{SOFT}=0.3$ . Buckling starts after 3.728 millsec at a displacement of 0.5592 inches.

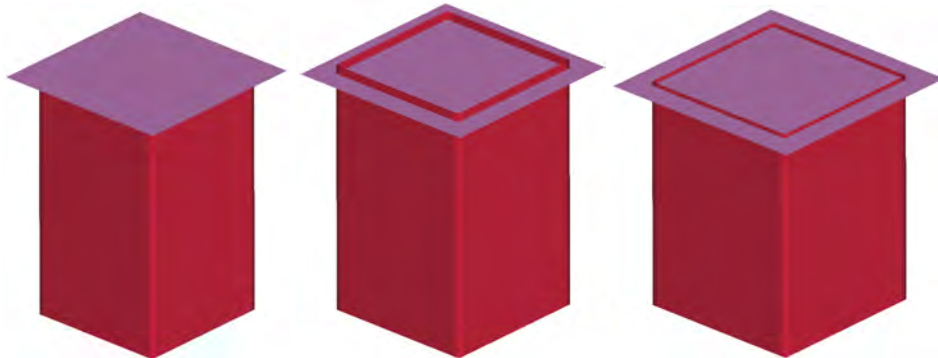


Figure 14. Example of a stable crushing of the tubular shape with  $\text{SOFT}=0.08$ . No buckling.



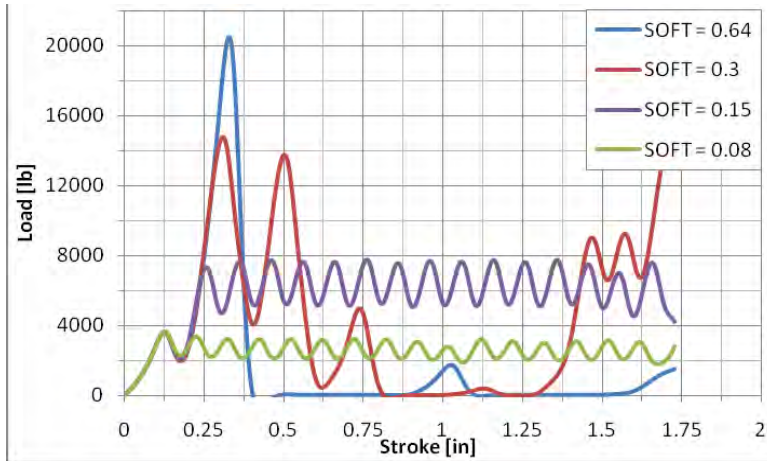


Figure 15. Load-displacement curves for the tube geometry with different SOFT values

Table VI. Process of finding the right SOFT value for each geometry type

Geometry Type	SOFT	EA	SEA [J/g]	% change w.r.t Test	Comment
<b>Square Tube</b>	Exp. Data	784.60	30.77		
	0.08	488.40	30.64	-0.4%	Stable
	0.09	549.09	34.45	11.9%	Stable
	0.10	639.26	40.11	30.3%	Stable
	0.15	1123.67	70.50	129.1%	Stable
	0.30	823.83	51.69	68.0%	Unstable @ 0.003728 [s]
<b>Large C-Channel</b>	Exp. Data	789.84	28.23	-	
	0.15	348.91	19.95	-29.3%	Stable
	0.20	454.58	25.99	-7.9%	Stable
	0.22	494.65	28.28	0.2%	Stable
	0.30	226.61	12.96	-54.1%	Unstable @ 0.003378 [s]
	0.64	219.80	12.57	-55.5%	Unstable @ 0.00233 [s]
<b>Small C-Channel</b>	Exp. Data	455.48	43.25	-	
	0.20	361.97	35.31	-18.4%	Stable
	0.235	440.17	42.93	-0.7%	Stable
	0.25	474.31	46.26	7.0%	Stable
	0.30	244.84	23.88	-44.8%	Unstable @ 0.005009 [s]
	0.64	105.32	9.47	-78.1%	Unstable @ 0.002912 [s]
<b>Small Corner</b>	Exp. Data	192.40	62.11	-	
	0.30	175.57	53.76	-13.4%	Stable
	0.32	182.26	55.81	-10.1%	Stable
	0.33	202.91	62.13	0.0%	Stable
	0.35	133.62	40.91	-34.1%	Unstable @ 0.005941 [s]
	0.40	75.51	23.12	-62.8%	Unstable @ 0.004194 [s]
	0.64	82.82	25.36	-57.0%	Unstable @ 0.002796 [s]
<b>Large Corner</b>	Exp. Data	504.8503	31.6	-	
	0.2	393.90	29.96	-5.2%	Stable
	0.21	420.02	31.94	1.1%	Stable
	0.22	436.99	33.23	5.2%	Stable
	0.64	82.82	6.54	-79.3%	Unstable @ 0.00233 [s]




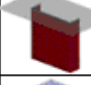
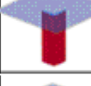

Table VI summarizes the trial and error procedure used to identify the suitable SOFT parameter to match the experimental curves for all five specimens shapes. It can be seen that although the material for these shapes is the same, the value of the SOFT parameter has to be varied for each shape in order to capture the experimental data. This bears the dual implication that the SOFT parameter is not a constant of the material, and that it cannot be predicted a priori. This in turn also means that LS-DYNA MAT54, although can be used successfully to reproduce the experimental results, it does not allow for a true predictive capability.

Summarized in Table VII are the values of SEA measured and simulated for each geometry, as well as a summary value of the optimal SOFT value as determined by trial and error. Figures 16-20 show the detailed geometry as well as the experimental and simulated L-D curves for all specimens considered.

Rearranging the values in Table VII it is possible to plot the experimental, and numerical, values of the SEA for each of the five geometries considered against the respective values of the SOFT parameter, Figure 21. It is very interesting to observe that there is a striking relationship between the SEA and this parameter, generally thought of as a numerical “tweaking” parameter. The relationship appears to be linear, and bears a strong connection to the plot of Figure 10, which shows SEA against degree of curvature.

It appears therefore that the SOFT parameter has therefore a physical meaning, associated to the degree of curvature of the cross-section, and hence its ability to perform well under axial crushing conditions. The more contoured (i.e. not flat) the section, the more stable it will be. Contoured sections tend to suppress the formation of delaminations, and is key in preventing the formation of large intact fronds. This in turn facilitates crushing and tearing over splaying/ frond formation, and hence it yields higher amounts of SEA. The smaller the delamination, the smaller the damage zone ahead of the crash front, and hence the higher the amount of pristine material available to dissipate energy. In LS-DYNA MAT54 this is captured by having higher values of SOFT parameters for more contoured geometries. The SOFT parameter can be physically related to the degree of damage that propagates ahead of the crashfront, and that affects the residual strength of the material that is about to become the crashfront.

Table VII. Dimensions, SEA and SOFT parameter value for each geometry type

Geometry type		Cross-sec A [in <sup>2</sup> ]	W [in]	Cross-sec L [in]	H [in]	Thickness [in]	SEA [J/g]	SOFT Calibrated
Tube		0.335156	2.3	4.6	4.1	0.07286	36.9	0.085
Large C-channel		0.378872	2.6	5.2	3.1	0.07286	42.7	0.23
Small C-channel		0.29144	2.6	4.0	3.1	0.07286	36.9	0.22
Small corner		0.087432	0.6	1.2	2.2	0.07286	62.30	0.33
Large Corner		0.306012	2.1	4.2	2.2	0.07286	31.6	0.21

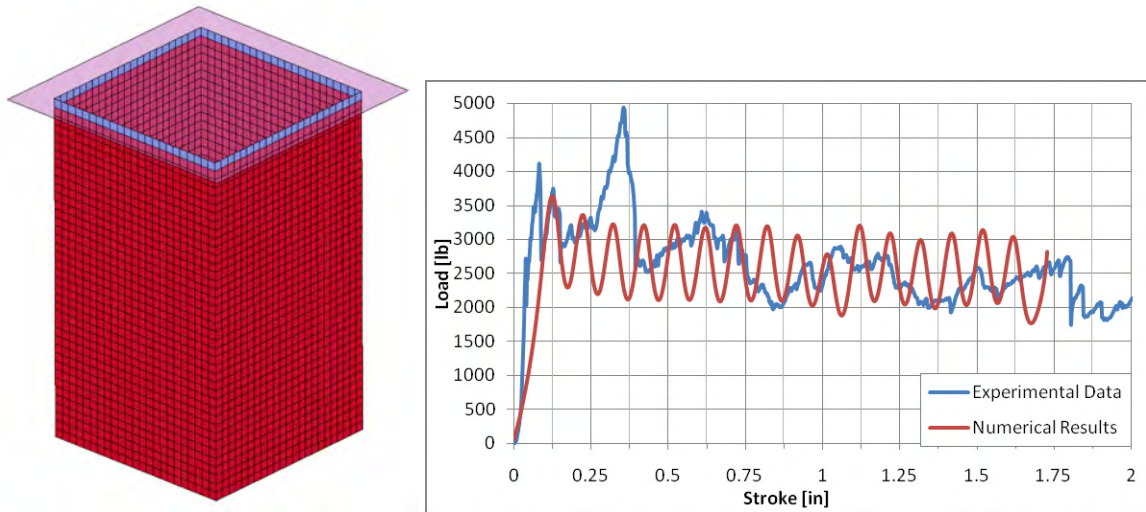


Figure 16. Model geometry and optimal Load-Displacement curve for the square tube specimen

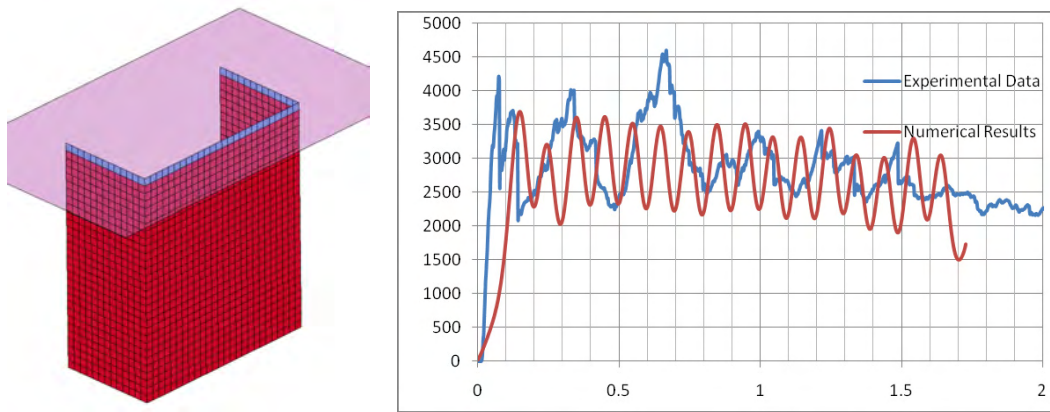


Figure 17. Model geometry and optimal Load-Displacement curve for the large C-Channel specimen.

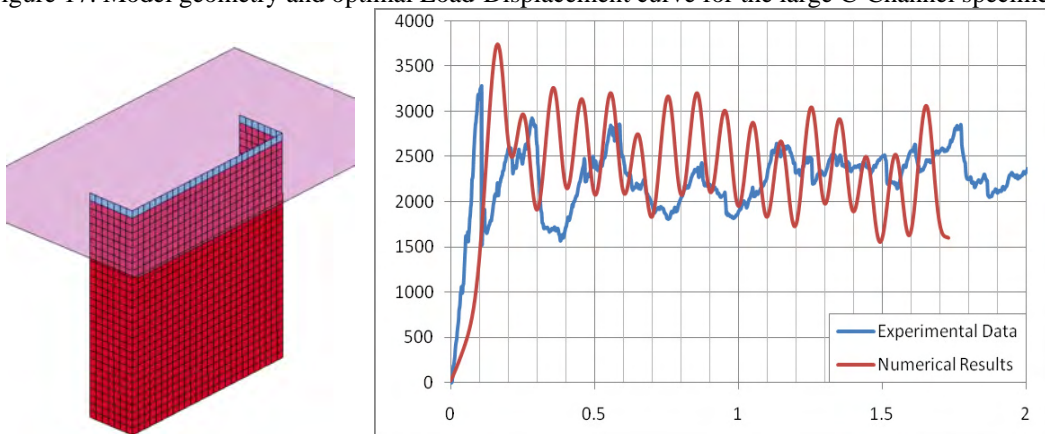


Figure 18. Model geometry and optimal Load-Displacement curve for the small C-Channel specimen.

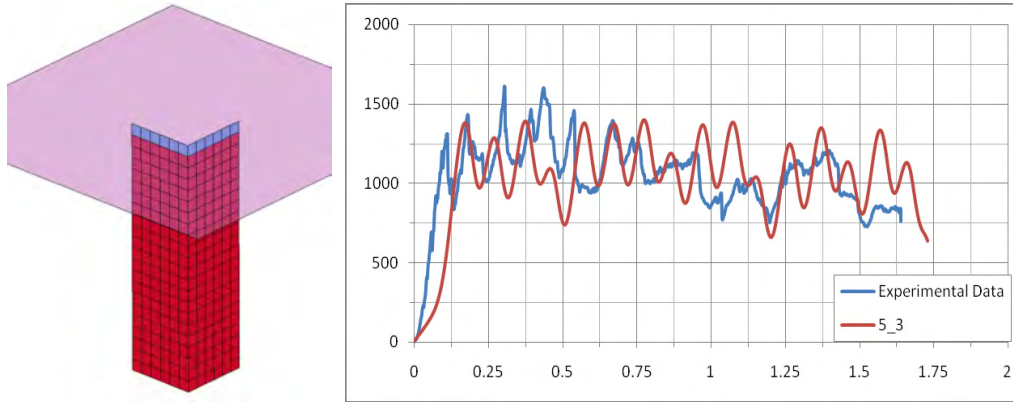


Figure 19. Model geometry and optimal Load-Displacement curve for the small corner specimen

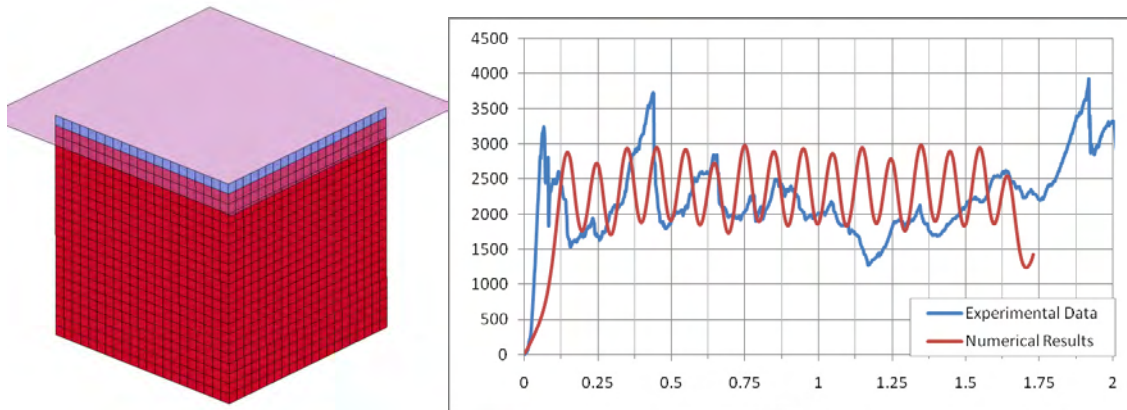


Figure 20. Model geometry and optimal Load-Displacement curve for the large Corner specimen

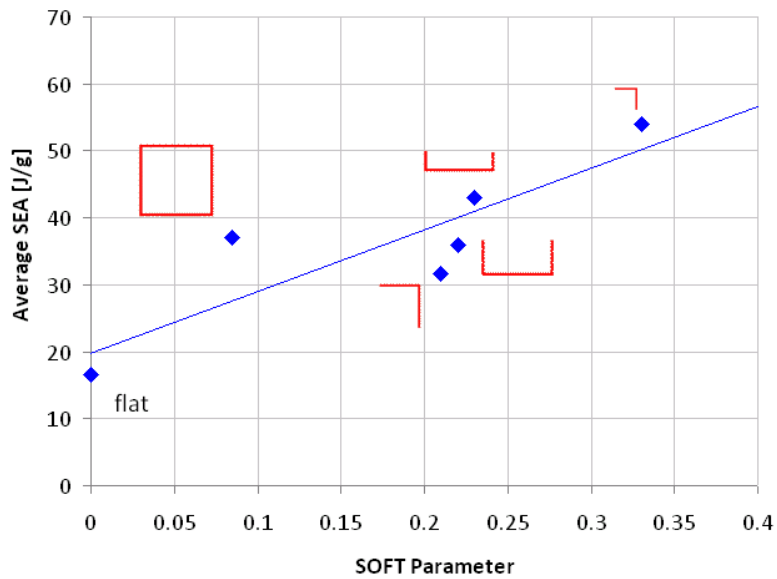


Figure 21. Linear relation between the SEA and the SOFT parameter

#### IV. Conclusions

Starting from a baseline of a fabric prepreg square tube, specimens with different geometric characteristics have been successfully crushed, including C-channels and corner elements of varying cross-section lengths. Laminate thickness, material system, manufacturing process, and test methodology used are kept constant throughout the study to specifically isolate the effects of cross-section geometry on the crush behavior for each specimen. Experimentally, it is found that for the material and lay-up considered, the small corner element is the most efficient in absorbing energy per unit mass compared to the other specimens with longer flanges. The more contoured the specimen (i.e. the least amount of flat segments), the higher the measured SEA. Fiber tensile fracture and tearing at the corners is responsible for the vast percentage of the energy absorbed, while frond formation and splaying of the large flat segments is responsible for a much lower percentage. In order to maximize the energy absorption it becomes fundamental to suppress delamination propagation and to minimize formation of large fronds while promoting fragmentation as failure mechanism. Numerically, it is found that the SOFT crash front parameter in LS-DYNA MAT54 is the single most influential modeling parameter, and that is capable of modifying the shape of the simulated load-displacement curve enough to perfectly match the experimental results. It is also found that the value of this parameter is not constant for the material, but needs to be varied for each specimen geometry. By trial and error, it is possible to identify a value of the SOFT parameter that can produce perfect agreement between simulated and experimental load-displacement curves. It is also found that this apparently “tweaking” parameter has in effect a deep physical interpretation. The higher the degree of curvature of the specimen, the more efficient it is in crushing by fragmentation rather than frond formation. The formation of large intact fronds is highly inefficient from an energy absorption standpoint, and is accompanied by the formation of long delamination in the specimen ahead of the crash front itself. This mechanism in turn acts as to create an effective damage length, which is not effective in absorbing energy. The extent of this damage length is captured by the value of the SOFT parameter, which reduces the strength of the row of elements directly ahead of the crash front.

#### Acknowledgments

The authors would like to express their gratitude to the Dr. Larry Ilcewicz, Curt Davies and Allan Abramowitz (Federal Aviation Administration), as well as Randy Coggeshall and Steve Precup (The Boeing Co.) for sponsoring the research. They would also like to thank the Crashworthiness Working Group of the CMH-17 (formerly known as MIL-HDBK-17). Leslie Cooke (Toray Composites of America) kindly supplied the material and specimens used in the study, and undergraduate student Enrique Gally Galgana was fundamental in the testing and graphics.

#### References

1. Carruthers, J.J., Kettle, A.P. and Robinson, A.M., "Energy Absorption Capability and Crashworthiness of Composite Material Structures: A Review", *Applied Mechanics Reviews*, 51, 1998, pp. 635-649.
2. Browne, A., Johnson, N., Botkin, M., "Dynamic crush response of RTM crash boxes", ASC 24<sup>th</sup> Technical Conference, Memphis, TN, September 2008.
3. Composite Materials Handbook (CMH-17), "Crashworthiness and Energy Management", Volume 3, Chapter 13, Rev. G
4. Johnson, A., "Determination of composite energy absorption properties", Proceedings of the 50<sup>th</sup> MIL-HDBK-17 Coordination Meeting - Crashworthiness Working Group, Chicago, IL, Jul. 2006.
5. Bolukbasi, A.O., Laananen, D.H., "Energy absorption in composite stiffeners", *Composites*, 26/4, 1995, pp. 291-301.
6. Feraboli, P., "Development of a corrugated test specimen for composite materials energy absorption" – *Journal of Composite Materials* - 42/3, 2008, pp. 229-256.
7. Feraboli, P., "Development of a modified flat plate test specimen and fixture for composite materials crush energy absorption" – *Journal of Composite Materials* - in press.
8. Lavoie, J.A., Morton, J., "Design and application of a quasistatic crush test fixture for investigating scale effects in energy absorbing composite plates", NASA CR 4526, July 1993.
9. Jackson, K., Morton, J., Lavoie, J., Boitnott, R., "Scaling of energy absorbing composite plates", *Journal of the AHS*, 39/1, 1994, pp. 17-23.

10. Tomblin, J., Sherraden, J., Seneviratne, W., Raju, K.S., "A-basis and B-basis Design Allowables for Epoxy-based prepreg Toray T700SC-12K-50C/ #2510 Plain Weave Fabric", AGATE-WP3.3-033051-131, Sept. 2002.
11. "T700SC 12K/ 2510 Plain Weave Fabric", Composite Materials Handbook (CMH-17), Volume 2, Chapter 4.2.38, Rev. G.
12. Hallquist JO, LS-DYNA Theoretical Manual, Livermore Software Technology Corporation, 2005.
13. Chang FK, Chang KY, A Progressive Damage Model for Laminated Composites Containing Stress Concentration, J Composite Materials, 21, 1987, 834-855.